Aerosol Size Distributions from Genetic Inversion of Polar Nephelometer Data*

B. R. LIENERT, J. N. PORTER, AND S. K. SHARMA

Hawaii Institute of Geophysics and Planetology, Honolulu, Hawaii

(Manuscript received 16 July 2002, in final form 6 March 2003)

ABSTRACT

It is shown that genetic inversions can be used to recover lognormal aerosol size distributions from multiangle optical scattering cross-section data measured by a polar nephelometer at a wavelength of 0.532 μm. The inversions can also be used to recover the absolute calibration factor of the polar nephelometer. The method is demonstrated by applying it to polar nephelometer data measured during the Shoreline Environment Aerosol Study (SEAS) at Bellows Beach on the island of Oahu, Hawaii. Also, the inverted size distributions are compared with those inferred from direct measurements by particle sizers during SEAS. At 0.532 μm, the polar nephelometer data are dominated by the effect of coarse-mode hydrated sea salt. Although the inversion was unable to place constraints on the accumulation-mode size distribution, the modeled size distribution provides a good description of optical scattering at wavelengths of 0.532 μm and above.

1. Introduction

Inversion of optical scattering cross-section measurements for aerosol size distributions allows critical optical parameters such as aerosol extinction, phase function, and lidar ratio to be predicted as a function of wavelength using Mie theory. However, due to the oscillatory variation of the Mie scattering cross sections with wavelength and aerosol size, such inversions can be highly nonunique (Post 1975). Uniqueness can be represented by the width of resolution kernels (Backus and Gilbert 1970). These are localized weighted averages of a continuously varying quantity (in this case aerosol size) that can be estimated by inverting a finite set of measured data (in this case, scattering cross sections). As the width of a resolution kernel is decreased, the error in its weighted average increases, resulting in a ''trade-off'' between resolution and error (Jackson 1972). Post (1975) showed that for the Mie scattering problem at multiple angles, the parameter resolution kernels giving reasonable errors were rather wide. He therefore proposed recovering distributions having a simple predefined shape, such as lognormal. We chose to use multimode lognormal distributions, as these have been shown by Porter and Clarke (1997) to adequately represent directly measured aerosol size distributions.

In a previous paper (Lienert et al. 2001), we showed how genetic inversion (Holland 1975; Goldberg 1989) could be used to recover multimodal lognormal aerosol size distributions from multiwavelength optical extinction data. The advantage of genetic inversion is that it explores a wide range of size distribution parameters, similar to the Monte Carlo method (Gentile 1998). In contrast, iterative inversion techniques (e.g., Oshchepkov et al. 2000; Dubovik and King 2000) iteratively apply corrections to a subjectively chosen starting set of parameters and therefore only explore a limited range of possible size distributions. Using repeated genetic inversions of calculated extinctions for unimodal and bimodal distributions, Lienert et al. (2001) used the inverted models to investigate uniqueness. They showed that for six-wavelength extinction data generated from a bimodal lognormal size distribution, the six recovered parameters of that distribution were highly nonunique unless the data were fitted to within 0.5%, which was considerably less than typical experimental errors.

In this paper, we use genetic inversion to investigate the inversion of multiangle scattering, similar to that measured using sky radiances (Dubovik and King 2000) or polar nephelometers (Barkey and Liou 2001). Since multiangle phase functions are also predicted by Mie theory, we suspected that similar problems of nonuniqueness could be present in the recovered distributions.

2. Description of the polar nephelometer

The instrument design follows the system of Winchester (1983), and an initial version is described by Porter et al. (1998). A 20-Hz frequency-doubled Nd:YAG laser (12 mJ per pulse at 532 nm) is used as the energy source, while a Hamamatsu H6779 miniature

* School of Ocean and Earth Science and Technology Contribution Number 6205.

Corresponding author address: Dr. B. R. Lienert, Hawaii Institute of Geophysics and Planetology, 2525 Correa Rd., Honolulu, HI 96822.
E-mail: lienert@mano.soest.hawaii.edu

© 2003 American Meteorological Society

Unauthenticated | Downloaded 12/08/24 05:29 AM UTC

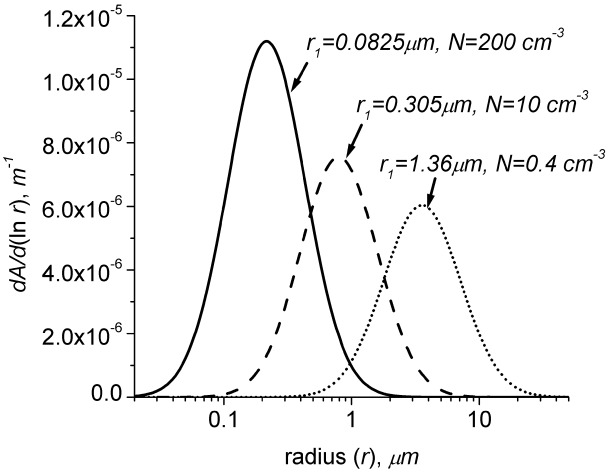

FIG. 1. Three lognormal area distributions approximately representing the accumulation (r_1 = 0.083 μm), coarse (r_1 = 0.305 μm), and large (r_1 = 1.36 μm) modes of aerosol size distributions.

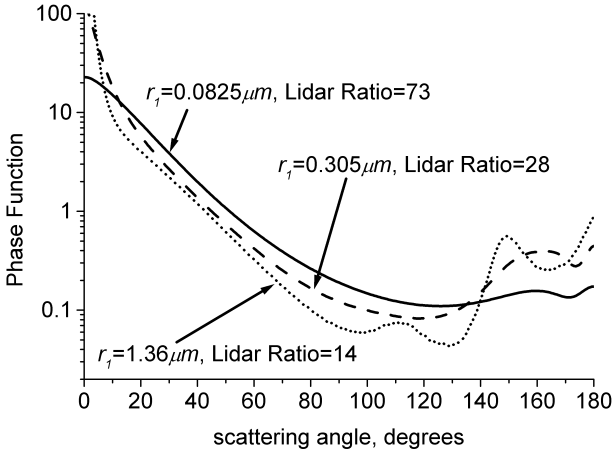

FIG. 2. Combined Mie and molecular scatter phase functions for three different amplitudes of the coarse-mode peak in Fig. 1. The lidar ratios, in sr, are also shown for each curve.

photomultiplier tube (PMT) is used as the detector. The PMT was fiber coupled to a collimating lens mounted on a moveable arm, 58 cm long, that rotates from ~2° to 178° in the plane of scatter, which is at right angles to the laser polarization direction. The moveable arm is connected to a computer-controlled stepper motor/position encoder. At each scattering angle, about 600 analog PMT output pulses are digitized and averaged using a 200-MHz digital oscilloscope. A variable-attenuation neutral density filter is used to reduce the signal at scattering angles close to the forward direction. A silicon diode system (IL1700 detector) was used to simultaneously monitor the scattered light at one fixed angle (45°). Dividing the scanning detector signal by the fixed detector signal corrected for variations in aerosol concentration and laser intensity. By integrating the energy in the PMT output pulses and correcting for the effective detector area and distance, the total differential scattering can be calculated at each angle.

3. Numerical methods

In order to explicitly define the measured quantities and size distribution parameters, which are defined in a number of different ways in the literature, we have included a summary of the theory we used to calculate angular differential scattering cross section, $d\sigma_i/d\Omega$, in the appendix. Using a program incorporating the routine of Bohren and Huffman (1983), $d\sigma_i/d\Omega_i$ was calculated at each radius and wavelength. The integral in Eq. (A10) was performed using quadrature integration (2000 points equally spaced in ln r from r = 0.002 to 200 μm). This number of points (400 per decade) was the minimum found necessary to prevent the occurrence of small oscillations in calculated values of P_1 and P_2 (defined in the appendix). The accuracy of the calculations was confirmed by calculating and comparing results for two models (Haze M and Cloud C-3) tabulated by Deirmendjian (1969).

To demonstrate how the Mie scattering phase functions vary with the type of size distribution, P_1 is plotted in Fig. 2 for the three unimodal area distributions in Fig. 1, with mean radii ranging from 0.0825 to 1.35 μm. We have plotted the size distributions as area, rather than number, as area is used to calculate extinction. We used a value of $1.36 + 0i$ for the refractive index of the aerosol particles, which is the value expected for a mass-weighted sea salt–water solution (Tang et al. 1997) at 85% relative humidity (RH), the value measured at the time of the polar nephelometer measurements (Masonis et al. 2003). It is apparent from Fig. 2 that the shapes of the resulting phase functions, as well as the values of the lidar ratios, are critically dependent on particle size, particularly at scattering angles of less than 30° and greater than 130°. Note, in particular, the characteristic undulations between angles of 90° and 130°, as well as between 140° and 180°, for the largest size distribution. The variation between 140° and 180°, frequently termed a rainbow, is characteristic of large spherically shaped aerosols (Bohren and Huffman 1983).

The phase functions calculated in Fig. 2 are for Mie scattering only. For our system the measured scatter was a combination of Mie scatter and molecular scatter. For a laser polarized at right angles to the plane of scattering, the molecular scatter, given by Eq. (A14), is independent of angle. Its contribution to the total scatter will therefore depend on the relative size of Mie scatter. This is illustrated in Fig. 3, where we have plotted total scatter normalized by integrated Mie scatter (i.e., the extinction for zero absorption) for one of the models in Fig. 1, with three different lognormal peak amplitudes giving values of scattering ranging from 1.7×10^{-5} to 4.4×10^{-4} m^{-1}. The depth of the ''valley'' between 40° and 140° gives an approximate indication of size of the aerosol extinction relative to the molecular scatter. Since the

Unauthenticated | Downloaded 12/08/24 05:29 AM UTC

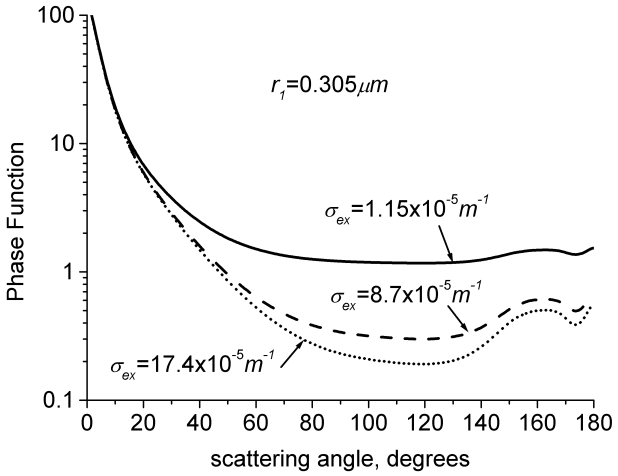

FIG. 3. Combined Mie and molecular scatter phase functions for three different amplitudes of the coarse-mode peak in Fig. 1. The theoretical extinctions (ext) (in m^{-1}) are also shown for each curve.

molecular scatter is known, it should be possible in principle to invert the combined scattering data for the polar nephelometer calibration factor, as well as for the aerosol size distribution causing Mie scattering.

The genetic inversion algorithm that we used is that described by Carroll (1996) and used in a previous paper by Lienert et al. (2001). Briefly, a random number generator is used to select the parameters for a lognormal size distribution having the form of Eq. (A5). The scattering predicted by Mie theory is calculated at each measurement angle, and the ''fitness'' of this distribution is calculated from its mean absolute error of fit to the measured data. Two sets of lognormal parameters are then concatenated into binary gene strings (parents), which are used to breed child solutions using randomly selected sections of each parent gene. Successive generations of children are then used to maximize the fitness. In this paper, for parameters such as the mutation fraction, population size, number of children, etc., we used the values given in Table 1. Note that we enabled the elitism feature, which ensures that the individual having the best fitness is always retained in subsequent iterations. In our previous paper, we defined the fitness as a specified standard deviation divided by the error of fit. In this paper, we use a different definition of fitness, which is similar to the inverse of a misfit function used in simulated annealing (e.g., Billings 1994), namely,

$$F(m, x) = \exp\left\{-\sum_{k=1}^{n}\left|\log\left[\frac{dP_{1,\text{observed}}(\theta)}{d\Omega}\right] - \log\left[\frac{dP_1(m, x, \theta)}{d\Omega}\right]\right| \Big/ n\right\}, \quad (1)$$

where $dP_{k,\text{observed}}(\theta)/d\Omega$ are n-measured differential scattering values and $dP_k(m, x, \theta)/d\Omega$ is given by Eq. (A8). The error of fit is then

TABLE 1. Parameters used in the genetic inversions.

Microgenetic algorithm enable	Yes
Population size	50
Number of parameters	4
Mutation fraction	0.04
Crossover probability	0.4
Tournament selection enable	Yes
Elitism enable	Yes
Parameter creep enable	No
Uniform selection enable	Yes
Niche selection enable	No
Number of children	1

$$\varepsilon = 1 - \log_e F(m, x). \quad (2)$$

We used the logarithm of the phase function in Eq. (1) to increase the relatively low weight of the scattering values observed at intermediate angles. We also found that by using the mean absolute error (the $M1$ norm) rather than the mean sum of squared data differences [the $M2$ norm used by Lienert et al. (2001)], we were able to significantly reduce the effect of large outliers on the solutions. Iterative inversions (e.g., Jackson 1972) calculate the parameter errors from the expected error in the data using the parameter covariance matrix, calculated from partial derivatives. Since the expected error in the data does not include errors due to inadequacy of the model being fitted, Eq. (2) provides a better estimate of the total error.

Since genetic inversion used a random number generator to choose individuals, it is not nearly as susceptible to becoming trapped in a local fitness maximum as are iterative processes. However, because all possible parameters are not explored, it is still possible that the global fitness maximum will not be found, particularly in highly nonunique problems such as this one. The only way to ensure that a truly global fitness maximum is recovered is to increase the population size to include all possible parameters that would make the calculation time prohibitive. Our approach is to repeat the inversions multiple times using different starting seeds for the random number generator (Lienert et al. 2001). In this way we obtain a family of solutions representing local fitness maxima in the solution space. We also no longer chose a convergence criterion based on fitness level (Lienert et al. 2001), as this decreased the exploration of the parameter space. In this study, we always ran 50 generations and used the five maximum fitness results for a total of 10 repeat inversions with different random number seeds.

As a test of the genetic inversion method, we applied it to artificial angular scattering data generated at a wavelength of 0.532 μm and at 1.25° intervals. We added random noise of ±3% (peak) to the scattering calculated for a unimodal distribution having $r_1 = 0.5$ μm and $\mu_1 = 2.0$. We then attempted to recover the original distribution using repeated genetic inversions. The results are plotted in Figs. 4 and 5 as number and area distributions, respectively. All of the recovered distri-

Unauthenticated | Downloaded 12/08/24 05:29 AM UTC

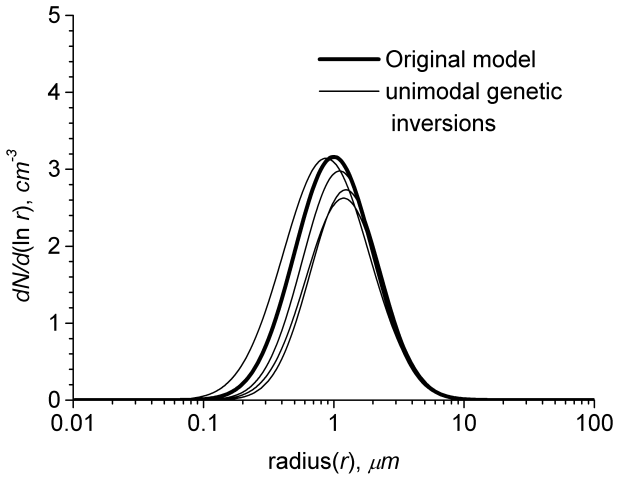

FIG. 4. Number distributions obtained by repeated genetic inversions of synthetic data generated by adding ±3% random noise to the theoretical phase functions calculated for a unimodal distribution (heavy solid curve).

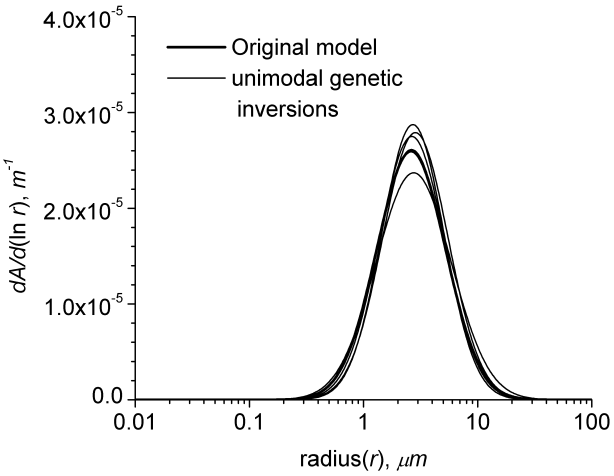

FIG. 5. The size distributions in Fig. 4 converted to cross-sectional area, $dA/d\ln r$.

butions had errors of fit [Eq. (2)] that agreed to within ±0.1%. Although there is considerable scatter in the number distributions, the area distributions are reasonably well grouped about the original distribution (heavy curve). The reason for the decrease in apparent scatter of the area distributions is that the data being inverted (scattering cross sections) depend on area rather than number. When a lognormal number distribution is converted to area, the lognormal median radius r_m shifts to a larger value $r_{m,p}$ according to

$$r_{m,p} = r_m \exp[p(\log_e \mu_i)^2] \quad (3)$$

(e.g., Tsay et al. 1991), with $p = 2$, which depends on the width μ_i of the number distribution. Although the distribution's width is unchanged by converting to area, different widths appear to be compensated for by changes in the peak amplitude N_i, with little effect on the angular scattering. The net effect is a larger apparent nonuniqueness in the inverted number distributions due to shifts in their central radii R_i that disappear when number is converted to area.

Because realistic size distributions are more adequately represented by a bimodal distribution (Porter and Clarke 1997), we repeated the numerical experiment with a bimodal distribution as the starting model. We chose the initial bimodal distribution to have similar mode radii and amplitudes to the distribution experimentally measured by Clarke and Kapustin (2003) during the Shoreline Environment Aerosol Study (SEAS). The resulting inverted area distributions are shown in Fig. 6. It is clear that although the coarse-mode peak ($r_1 = 1.5$ μm) is well recovered, the amplitudes of the accumulation modes ($r_1 = 0.15$ μm) are too low, indicating that the polar nephelometer data (at 532 nm) are insensitive to the accumulation mode when it is relatively small.

4. Inversion of Bellows Beach data

The polar nephelometer was operated from 0400 to 0600 UTC on 28 April 2000. The nephelometer was mounted on top of the lidar container, about 5 m above sea level and 30 m from the breaking waves on the beach. During SEAS, the polar nephelometer was a prototype version and an accurate calibration was not available. As pointed out in the previous section, we found that it was possible to recover the system calibration factor as an additional unknown parameter in the genetic inversions. The measured scattering data (squares) appear in Fig. 7. The area distribution models for five repeat unimodal inversions are shown in Fig. 8. The refractive index used for these models was 1.40, which

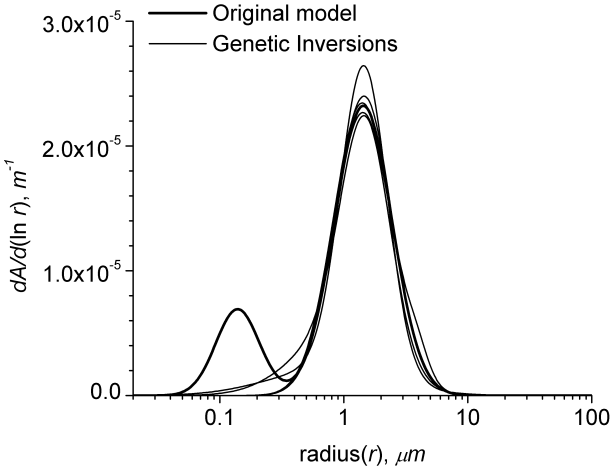

FIG. 6. Cross-sectional area distributions obtained by repeated genetic inversions of synthetic data generated by adding ±3% random noise to the theoretical phase functions calculated for a bimodal distribution (heavy solid curve). The inverted models (light curves) do not show an obvious second mode due to the low amplitudes of the accumulation modes and their closeness of their central radii to the coarse-mode peak radii.

Unauthenticated | Downloaded 12/08/24 05:29 AM UTC

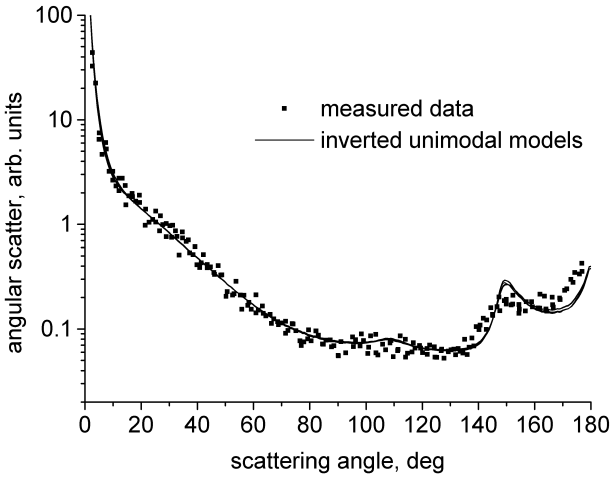

FIG. 7. Measured data (squares) collected at Bellows Beach at 1200 UTC 27 Apr 2000. The solid curves are those predicted by the unimodal genetic inversion models in Fig. 8 and Table 2.

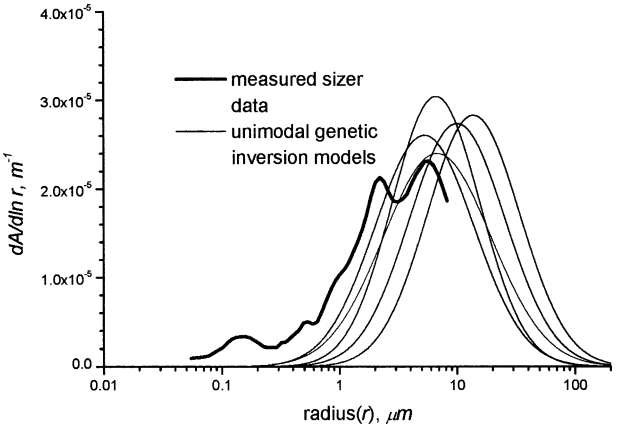

FIG. 8. Cross-sectional area distribution models obtained by five repeated genetic inversions of the data in Fig. 7 (solid lines). Also shown (squares) are the aerosol sizer data of Clarke and Kapustin (2003) converted to cross-sectional area.

was the value that gave the minimum error of fit in repeated inversions at steps of 0.01 from $1.38 + 0i$ to $1.42 + 0i$ in refractive index. It is not clear why this value is higher than the refractive index of 1.36 calculated for the measured RH of 85%. Also shown are the aerosol sizer measurements of Clarke and Kapustin (2003) corrected to ambient RH, cross section to surface area, and $dN/d\log D$ to $dN/d\ln r$. The theoretical angular scatters predicted by the five unimodal models are shown as solid curves in Fig. 7. The distribution parameters, calculated extinctions, lidar ratios L, calibration factors C, and errors of fit ε for the five models appear in Table 2.

Although the theoretical scattering values (Fig. 7) agree well with the experimental data at angles of up to 135°, there is a systematic deviation at angles larger than this. To investigate whether this is due to an incorrect value of the aerosol refractive index, in Fig. 9 we have plotted the theoretical scattering for one of the inverted models is Fig. 8 at three different values of refractive index. Figure 9 demonstrates that the model misfit cannot be accounted for by varying the refractive index. The other possibility is the presence of nonspherical aerosols. Although the hydrated coarse-mode salt droplets are spherical, the accumulation mode, which Clarke and Kapustin (2003) concluded was due to volcanic ash, could be causing the misfit. Although we have demonstrated that the polar nephelometer data are insensitive to the accumulation mode (Fig. 6), this conclusion may not be valid if the aerosols are nonspherical. We experimented with adding an additional spherical mode with a similar radius to that measured by Clarke and Kapustin (2003) having a refractive index of $1.6 + 0.01i$, but were still unable to fit the data at angles of greater than 135° without seriously degrading the fit at angles of less than 30°.

5. Discussion

The inverted area distributions in Fig. 8 compare reasonably well in both amplitude and radius with the sizer data (heavy curve) of Clarke and Kapustin (2003), although they do not include the accumulation-mode aerosols. However, Clarke and Kapustin, in a plot of aerosol area times Mie cross-section efficiency, show that the accumulation-mode contribution is less than 5% of the total scattering. Our mean calculated extinctions (Table 2) are similar to the values inferred from scanning lidar over breaking waves (Porter et al. 2003) and to inlet-corrected nephelometer measurements made during the SEAS experiment (Clarke and Kapustin 2003). The fairly large scatter in all three of the unimodal parameters (Table 2) is due to nonuniqueness in the inversion, as the errors of fit are close to identical. This nonuniqueness can only be reduced by improving the scatter in

TABLE 2. Parameters and their means for the five inverted unimodal distributions shown in Fig. 8.

N_1 (cm^{-3})	R_1 (μ)	M_1	σ_{ex} m^{-1}	L (sr)	C	ϵ
1.02	1.34	2.47	1.36×10^{-4}	14.0	3.53×10^{4}	9.4%
2.00	0.87	2.55	1.39×10^{-4}	14.2	3.36×10^{4}	9.4%
1.92	1.63	2.63	1.36×10^{-4}	14.3	3.43×10^{4}	9.4%
0.96	3.03	2.36	1.39×10^{-4}	13.9	3.45×10^{4}	9.4%
1.54	1.46	2.87	1.35×10^{-4}	14.5	3.49×10^{4}	9.4%
1.5 ± 0.5	1.7 ± 0.8	2.6 ± 0.2	$(1.37 \pm 0.02) \times 10^{-4}$	14.2 ± 0.2	$(3.45 \pm 0.06) \times 10^{4}$	9.4%

Unauthenticated | Downloaded 12/08/24 05:29 AM UTC

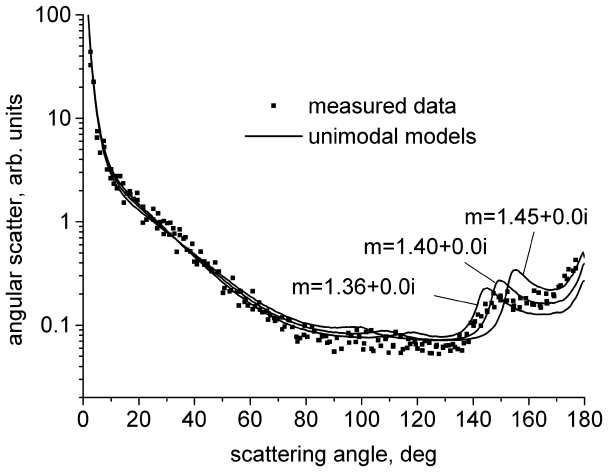

FIG. 9. Theoretical scattering curves (solid curves) calculated for one of the unimodal models in Fig. 8 at a number of different refractive indices. The measured data are again shown as squares.

the measured data or increasing their number. We have since reduced some of this error by using a logarithmic amplifier (Lienert et al. 2002). The lidar ratios we calculated from the different aerosol models in Table 1 ranged from 13.9 to 14.5. These are significantly lower than the lidar ratios of 20–30 measured directly at an altitude of 11 m by Masonis et al. (2003). However, our instrument was directly measuring large salt spray droplets carried up from breaking waves on the beach, which may not have been detected by the other instruments because of inlet losses (Porter and Clarke 1997).

APPENDIX

Mie Scattering Calculations

Mie's solution (Mie 1908; van de Hulst 1981) for a spherical particle of radius r microns (μm) gives the complex scattering components $S_1(m, x, \theta)$ and $S_2(m, x, \theta)$, perpendicular and parallel, respectively, to the plane of scattering, where m is the complex refractive index of the particle, θ is the scattering angle (in the plane of scatter), $k = 2\pi/\lambda$, λ is the wavelength (μm), and $x = kr$. For unit incident radiation flux polarized either perpendicular ($j = 1$) or parallel ($j = 2$) to the scattering plane, respectively, the differential angular scattering cross sections are then

$$\frac{d\sigma_{\text{Mie},i}(m, x, \theta)}{d\Omega} = \frac{|S_j(m, x, \theta)|^2}{k^2} \ (\mu\text{m sr}^{-1}), \quad \text{(A1)}$$

where Ω is the solid angle. Note that we have used a derivative with respect to Ω to make the distinction between total and differential scattering cross sections explicit. Integrating Eq. (A1) over Ω gives the total scattering cross section as

$$\sigma_{\text{Mie},j}(m, x) = \frac{2\pi}{k^2} \int_0^\pi |S_j(m, x, \theta)|^2 \sin\theta \, d\theta \quad (\mu\text{m}^2). \quad \text{(A2)}$$

Normalizing Eq. (A2) by the cross-sectional area of the spherical particle πr^2 gives the (dimensionless) integrated scattering efficiency

$$Q_{\text{Mie},i}(m, x) = \frac{2}{x^2} \int_0^\pi |S_j(m, x, \theta)|^2 \sin\theta \, d\theta. \quad \text{(A3)}$$

For comparison with measurements by other instruments such as lidar, nephelometers, etc., it is also useful to calculate the extinction cross section (van de Hulst 1981):

$$\sigma_{\text{ext}}(m, x) = \frac{4\pi}{k^2} \text{Re}\{S(m, x, 0)\} \quad (\mu\text{m}^2), \quad \text{(A4)}$$

where $S(m, x, 0) = S_1(m, x, 0) = S_2(m, x, 0)$. For the case of zero absorption [Im $(m) = 0$], $\sigma_{\text{ext}}(m, x) = \sigma_{\text{Mie},i}(m, x)$.

In order to extend Eqs. (A1)–(A4) to an assemblage of spherical particles having different radii, we assumed an M-modal lognormal distribution in $\ln r$ (Lienert et al. 2001):

$$\frac{dN}{d\ \ln r} = \sum_{i=1}^{M} N_i \exp\left(\frac{-(\ln r - \ln R_i)^2}{2(\ln\mu_i)^2}\right) \quad (\text{m}^{-3}), \quad \text{(A5)}$$

where N_t is the peak number concentration (m^{-3}), R_t is the central radius, and $\ln\mu_i$ is the spread in each mode (we use μ_i rather than σ_i for the spread to distinguish it from the scattering cross section). We have also defined N_i as the peak, rather than the integrated number concentration, to keep it independent of σ_i. The advantage of the lognormal distribution is that it has the same form in number, area and volume distributions.

The total differential scattering cross sections are now obtained by integrating Eq. (A1) over $\ln r$ to give

$$\frac{d\sigma_{\text{Mie},j}(\theta, m)}{d\Omega} = \frac{10^{12}}{k^2} \int |S_j(m, x)|^2 \sum_{i=1}^{M} N_i \exp\left[\frac{-(\ln r - \ln R_i)^2}{2(\ln\mu_i)^2}\right] d\ln r \quad (\text{m}^{-1}\ \text{sr}^{-1}), \quad \text{(A6)}$$

where the factor of 10^{12} results from converting k from μm^{-1} to m^{-1}. Similarly, the total integrated scattering (m^{-1}) becomes

$$\sigma_{\text{Mie},j}(m) = \frac{10^{12}}{k^2} \int Q_{\text{Mie},j}(m, x)\pi r^2 \sum_{i=1}^{M} N_i \exp\left[\frac{-(\ln r - \ln R_i)^2}{2(\ln\mu_i)^2}\right] d\ln r \quad (\text{m}^{-1}). \quad \text{(A7)}$$

Unauthenticated | Downloaded 12/08/24 05:29 AM UTC

The differential scattering efficiencies (sr^{-1}; phase functions), given by

$$\frac{dP_{\mathrm{Mie},j}(\theta, m)}{d\Omega} = \frac{1}{\sigma_{\mathrm{Mie},j}(m)} \frac{d\sigma_{\mathrm{Mie},j}(\theta, m)}{d\Omega}, \quad \text{(A8)}$$

are also useful to calculate. The ratio of total scattering to the scattering at 180°, termed the lidar ratio, is then

$$L_j(m) = \sigma_{\mathrm{ext}}(m)/[d\sigma_{\mathrm{Mie},j}(180, m)/d\Omega] \quad \text{(sr)} \quad \text{(A9)}$$

where the total extinction (m^{-1}) is given by

$$\sigma_{\mathrm{ext}}(m) = 10^{12} \int Q_{\mathrm{ext}}(m, x)\pi r^2 \sum_{i=1}^{M} N_i \exp\left[\frac{-(\ln r - \ln R_i)^2}{2(\ln \mu_i)^2}\right] d\ln r \quad (\mathrm{m}^{-1}). \quad \text{(A10)}$$

When the absorption is zero, $\sigma_{\mathrm{Mie},j} = \sigma_{\mathrm{ext}}$ and

$$L_j(m) = \frac{1}{dP_j(180, m)/d\Omega}. \quad \text{(A11)}$$

In the case of nonpolarized light, it is easily shown that the equations for the total integrated scattering efficiency, $Q(m)$, and the differential phase function, $dP(\theta, m)/d\Omega$, are given by

$$Q(m) = [Q_1(m) + Q_2(m)]/2 \quad \text{and} \quad \text{(A12)}$$

$$\frac{dP(\theta, m)}{d\Omega} = \frac{\left[Q_1(m)\frac{dP_1(\theta, m)}{d\Omega} + Q_2(m)\frac{dP_2(\theta, m)}{d\Omega}\right]}{Q(m)}. \quad \text{(A13)}$$

The corresponding molecular (Rayleigh) scattering equations for linear polarization are (e.g., Coulson 1988)

$$\frac{d\sigma_{\mathrm{mol},1}}{d\Omega} = \frac{24 \times 10^{24}\pi^3}{N\lambda^4}\left|\frac{m_a^2 - 1}{m_a^2 + 2}\right|^2 \frac{3}{8\pi} \quad \text{(A14)}$$

at right angles to the scattering plane and

$$\frac{d\sigma_{\mathrm{mol},2}}{d\Omega} = \frac{24 \times 10^{24}\pi^3}{N\lambda^4}\left|\frac{m_a^2 - 1}{m_a^2 + 2}\right|^2 \frac{3}{8\pi}\cos^2\theta \quad (\mathrm{m}^{-1}\ \mathrm{sr}^{-1}) \quad \text{(A15)}$$

perpendicular to the scattering plane, where m_a is the atmospheric refractive index (close to 1 for air) and N is the molecular concentration (in m^{-3}), which is calculated as a function of altitude using standard corrections (Coulson 1988). Here, Eqs. (A14) and (A15) have been separately normalized to give unit integrals over solid angle, rather than normalizing their sum, as is done in the unpolarized case (e.g., Coulson 1988).

REFERENCES

Backus, G., and F. Gilbert, 1970: Uniqueness in the inversion of inaccurate gross earth data. *Philos. Trans. Roy. Soc. London,* **266,** 123–130.

Barkey, B., and K. N. Liou, 2001: Polar nephelometer for light-scattering measurements of ice crystals. *Opt. Lett.,* **26,** 232–234.

Billings, S. D., 1994: Simulated annealing for earthquake location. *Geophys. J. Int.,* **118,** 680–692.

Bohren, C. F., and D. R. Huffman, 1983: *Absorption and Scattering of Light by Small Particles.* Wiley Interscience, 530 pp.

Carroll, D. J., 1996: Chemical laser modeling with genetic algorithms. *AIAA J.,* **34,** 338–346.

Clarke, A. D., and V. N. Kapustin, 2003: The Shoreline Environment Aerosol Study (SEAS): A context for marine aerosol measurements influenced by a coastal environment and long-range transport. *J. Atmos. Oceanic Technol.,* **20,** 1351–1361.

Coulson, K. L., 1988: *Polarization and Intensity of Light in the Atmosphere.* A. Deepak, 596 pp.

Deirmendjian, D., 1969: *Electromagnetic Scattering on Spherical Polydispersions.* Elsevier, 290 pp.

Dubovik, O., and M. D. King, 2000: A flexible algorithm for retrieval of aerosol optical properties from sun and sky radiance measurements. *J. Geophys. Res.,* **105,** 20 673–20 696.

Gentile, J. E., 1998: *Random Number Generation and Monte Carlo Methods.* Springer-Verlag, 247 pp.

Goldberg, D. E., 1989: *Genetic Algorithms in Search, Optimization and Machine Learning.* Addison-Wesley, 412 pp.

Holland, J. H., 1975: *Adaptation in Artificial and Natural Systems.* University of Michigan Press, 183 pp.

Jackson, D. D., 1972: Interpretation of inaccurate, insufficient and inconsistent data. *Geophys. J. Roy. Astron. Soc.,* **28,** 97–109.

Lienert, B. R., J. N. Porter, and S. K. Sharma, 2001: Repetitive genetic inversion of optical extinction data. *Appl. Opt.,* **40,** 3417–3427.

——, ——, ——, N. Ahlquist, and D. Harris, 2002: A 50-MHz logarithmic amplifier for use in lidar measurements. *J. Atmos. Oceanic Technol.,* **19,** 654–657.

Masonis, S. J., T. L. Anderson, D. S. Covert, V. Kapustin, A. D. Clarke, S. Howell, and K. Moore, 2003: A study of the extinction-to-backscatter ratio of marine aerosol during the Shoreline Environment Aerosol Study. *J. Atmos. Oceanic Technol.,* **20,** 1388–1402.

Mie, G., 1908: Beiträge zuroptic trüber medien spieziell kolloidaler metallösungen. *Ann. Phys.,* **25,** 377–445.

Oshchepkov, S., H. Isaka, J.-F. Gayet, A. Sinyuk, F. Auriol, and S. Havemann, 2000: Microphysical properties of mixed-phase and ice clouds retrieved from in *in situ* airborne ''Polar Nephelometer'' measurements. *Geophys. Res. Lett.,* **27,** 209–212.

Porter, J., and A. D. Clarke, 1997: Aerosol size distribution models based on in situ measurements. *J. Geophys. Res.,* **102,** 6035–6045.

——, T. F. Cooney, and C. Motell, 1998: Coastal aerosol phase function measurements with a custom polar nephelometer. *Proc. ONR Ocean Optics XIV Conf.,* Kona, HI, Office of Naval Research, 5.

——, B. R. Lienert, S. K. Sharma, E. Lau, and K. Horton, 2003: Vertical and horizontal aerosol scattering fields over Bellows Beach, Oahu, during the SEAS experiment. *J. Atmos. Oceanic Technol.,* **20,** 1375–1387.

Post, M. J., 1975: Limitations of cloud droplet size distribution by Backus–Gilbert inversion of optical scattering data. *J. Opt. Soc. Amer.,* **5,** 483–486.

Tang, I. N., K. Tridico, and K. H. Pung, 1997: Thermodynamic and

Unauthenticated | Downloaded 12/08/24 05:29 AM UTC

optical properties of sea-salt aerosols. *J. Geophys. Res.,* **102,** 23 269–23 275.

Tsay, S.-C., G. L. Stephens, and T. J. Greenwald, 1991: An investigation of aerosol microstructure on visual air quality. *Atmos. Environ.,* **25A,** 1039–1053.

van de Hulst, H. C., 1981: *Light Scattering by Small Particles.* Dover, 470 pp.

Winchester, J. W., 1983: Phase function measurements of premier grade diesel fuel smoke. *Opt. Eng.,* **22,** 40–44.

Unauthenticated | Downloaded 12/08/24 05:29 AM UTC